

# Ultrathin P(NDI2OD-T2) Films with High Electron Mobility in Both Bottom-Gate and Top-Gate Transistors

Thomas Steckmann, Indunil Angunawela, Somayeh Kashani, Youqin Zhu, Masrur M. Nahid, Harald Ade, and Abay Gadisa\*

Ultrathin organic films (typically < 10 nm) attracted great attention due to their (semi)transparency and unique optoelectronic properties that benefit applications such as sensors and flexible electronics. At the core of that, achieving high mobility in an ultrathin film is essential for the efficient operation of relevant electronic devices. While the state-of-the-art material systems, e.g., P(NDI2OD-T2) also known as N2200 can achieve high mobility in a thin film (typically > 20 nm), multitudinous challenges remain in processing an ultrathin film exhibiting desired charge transport morphology within a preferred thickness limit. Here, high electron mobility (a tenfold increase compared to annealed spin-coated films) is reported in both the top and bottom-gate configuration organic field-effect transistors comprising ultrathin N2200 films produced with a water-floating film transfer method. A range of characterization techniques are used to investigate these ultrathin films and their microstructure, and conclude that favorable edge-on polymer orientation at the top as well as throughout the ultrathin film thickness and the quality of  $\pi$ - $\pi$  ordering as captured by the largest coherences length resulted in this high mobility in N2200 ultrathin films, in stark contrast to the commonly observed microstructural gradient in spin-coated thin films. The results provide new insight into the electronic and microstructural properties of thin films of organic semiconductors.

## 1. Introduction

The current generation of organic field-effect transistors (OFETs) is rapidly approaching performance standards that are required to realize functioning electronics devices. In particular, recent achievements of enhanced charge carrier mobility, current on/off ratio, improved stability, and acceptably small threshold voltages are important milestones in the quest for developing commercially viable OFETs.<sup>[1,2]</sup> While not likely to challenge the performance of silicon transistors in computing applications,

OFETs offer unique advantages in applications such as flexible and wearable electronics,<sup>[3]</sup> and transparent or translucent devices in display technology.<sup>[4]</sup> Each of these applications can be addressed by focusing not only on the materials used to fabricate OFETs, but also the fabrication methods to prioritize the large area and efficient fabrication of OFETs in the ultrathin (less than 10 nm) regime. Ultrathin devices can offer numerous advantages: reducing the thickness of the channel increases the elastic modulus of the OFET in wearable and flexible electronics,<sup>[3]</sup> while their large surface area in contact with the environment makes them excellent candidates to develop highly sensitive gas and chemical sensors.<sup>[5]</sup> In OFETs with an ultrathin active layer, the whole transistor channel can easily be accessed by an external environment (gas or chemical), which significantly improves the diffusion of the analytes through the organic active layer to the sensing interface (the semiconductor/dielectric interface), leading to high sensitivity.<sup>[5]</sup> Additionally, due to the scarcity of transparent conju-

gated semiconducting polymers, a viable approach to fabricate transparent devices is to reduce the amount of available light-absorbing material by reducing the film thickness. Thinner devices necessarily use less material, which further reduces the fabrication cost of OFETs and makes them more appealing for industrial adoption and more accessible for everyday electronics.

To realize ultrathin films, one of the best approaches is the floating film transfer method (FTM), also known as air-liquid interfacial self-assembly<sup>[6–8]</sup> or the spontaneous spreading phenomenon,<sup>[9]</sup> which takes advantage of the spreading coefficient between a solvent and liquid substrate to spontaneously spread a thin, uniform polymer film across the surface of the substrate (see Figure S1, Supporting Information). Once dried, the film can be directly transferred to a substrate. Prior works that primarily focused on manipulating the fabrication conditions of the films have successfully demonstrated the viability of the method both as a highly scalable method capable of roll-to-roll fabrication,<sup>[10]</sup> and the ability to control film characteristics and self-annealing by varying the fabrication conditions.<sup>[11–13]</sup> It is worth mentioning that several film assembly methods were utilized in the past to form ultrathin OFET films.<sup>[14–18]</sup>

T. Steckmann, I. Angunawela, S. Kashani, Y. Zhu, M. M. Nahid, H. Ade, A. Gadisa  
Department of Physics  
Organic and Carbon Electronics Labs (ORaCEL)  
North Carolina State University  
Raleigh, NC 27695, USA  
E-mail: agdinku@ncsu.edu, abaygd@gmail.com

 The ORCID identification number(s) for the author(s) of this article can be found under <https://doi.org/10.1002/aelm.202101324>.

DOI: 10.1002/aelm.202101324

In general, mobilities exceeding  $20 \text{ cm}^2 \text{ V}^{-1} \text{ s}^{-1}$  were reported for OFETs employing well-controlled film morphology.<sup>[19–21]</sup> To achieve high OFET performance, it is critical to acquire optimized film microstructure near the polymer/dielectric interface. Specifically, edge-on preferential crystal orientation<sup>[22]</sup> and substantially high coherence length<sup>[23]</sup> are critically preferred to realize efficient charge transport across the transistor channel. An edge-on orientation can be achieved through controlled film processing protocols such as solvent treatment,<sup>[24–26]</sup> thermal annealing<sup>[27]</sup> unidirectional solution processing,<sup>[28–30]</sup> and solvent-assisted friction transfer methods.<sup>[31]</sup> Using the Langmuir–Schaefer (LS) film casting method, Fabiano et al. demonstrated monolayer polymer OFETs showing preferentially edge-on orientation and thickness-dependent mobility.<sup>[32]</sup> The later authors, using the high-mobility semiconducting n-type polymer poly{[N,N9-bis(2-octyl dodecyl)-naphthalene-1,4,5,8-bis(dicarboximide)-2,6-diyl]-alt-5,59-(2,29-bithiophene)} (P(NDI2OD-T2), Polyera ActivInk N2200),<sup>[33]</sup> have successfully analyzed the performance of N2200/poly(methyl methacrylate) top-gate bottom-contact (TGBC) OFETs with only a single monolayer,<sup>[32,34]</sup> and subsequent work has demonstrated that LS film fabrication only allows for the creation of film molecular layers which are confined to 2D charge transport within only the interfacial, mostly edge-on polymer molecular layer.<sup>[35]</sup> According to the work of Salleo and co-workers, melt annealing of N2200 films<sup>[36]</sup> lead to a predominantly edge-on orientation and a two-fold increase in crystallinity in the bulk though this change is uncorrelated with transistor operation, indicating a different morphology is maintained at the organic/insulator interface. The highest mobilities in N2200 have been observed in top-gate bottom-contact device configurations, including the observation of record mobilities over  $1 \text{ cm}^2 \text{ V}^{-1} \text{ s}^{-1}$ ,<sup>[37]</sup> while bottom-gate bottom-contact (BGBC) devices often suffer from significant performance drops. This interface-dependent transport is mostly attributed to the vertical gradient in polymer orientation.<sup>[38]</sup>

Herein, we analyze the charge transport properties and thickness control of N2200 transistors fabricated using FTM. The results of this study indicate ultrathin N2200 OFETs exhibit high mobilities both in the top and bottom gate OFETs. This result is contrasted with prior attempts at fabricating films via sequential monolayer deposition of the Langmuir–Schaefer method where the 2D charge transport in a bilayer LS film was detrimental to electron mobility.<sup>[32]</sup> In comparison, FTM allows for fabricating ultrathin films with no such mobility handicap. Indeed, FTM films have comparable to or even exceeded the mobility typically recorded in spin-coated devices. Our finding highlights the possibility of achieving high performance in thin-film electronics, by exploring the role of thickness on molecular orientation and order.

## 2. Results and Discussions

### 2.1. Film Formation

Films of N2200 were formed by drop-casting 10 to 50  $\mu\text{L}$  of a warm polymer solution in p-xylene onto room temperature water (see Figure S1, Supporting Information). P-xylene is relatively insoluble in water and has a high spreading coefficient

among good solvents for N2200.<sup>[37,39]</sup> The high spreading coefficient and relatively slow evaporation ensure a uniform spreading of polymer solution across the water surface before solvent evaporation is complete. It is also noted that warm polymer solution ( $70 \text{ }^\circ\text{C}$ ) slows down polymer aggregation preceding film formation. Films cast from solvents such as chloroform, dichlorobenzene, and 1,2-dichlorobenzene lack continuity and uniformity. Full processing details can be found in the Experimental Section.

Films were transferred to either glasses or transistor substrates for investigating their optical, microstructural, and electrical properties. Ultrathin films of N2200, down to a few molecular layers of thicknesses of  $\approx 2.6 \text{ nm}$  as in Figure S2 of the Supporting Information, were produced. Film thickness was controlled via manipulation of three parameters in the FTM film formation: the solution concentration, the volume of the deposited solution, and the surface area of the liquid substrate determined by the area of the container used for casting. Transferring films from the water surface to substrates requires the usage of a highly hydrophobic substrate to prevent intrusion of water onto the substrate: in these experiments, the substrates are treated with octadecyltrichlorosilane (OTS), which also has beneficial charge transport properties in transistors.<sup>[40]</sup>

### 2.2. OFET Charge Transport

The charge transport properties of the N2200 thin films were studied in both top-gate and bottom-gate bottom-contact OFETs. The current–voltage output characteristics of the transistors are displayed in Figures S3 and S4 of the Supporting Information. The electron mobility of the N2200 films is displayed in **Figure 1** and **Table 1**. As inferred from Figure 1 and Table 1, better electron mobility is achieved in the ultrathin films while thicker films seem to reduce charge transport regardless of device configuration. In fact, the mobility of the thickest floated films ( $\approx 30 \text{ nm}$ ) and the best spin-cast films are nearly the same in both TGBC and BGBC OFETs. It is well known that BGBC OFETs give low mobility in N2200 films due to unfavorable material structure at the gate dielectric/N2200 interface.<sup>[30,37]</sup> Because of this restriction, TGBC OFETs are often employed to characterize the charge transport of N2200. It is noted that the thick floated sample gives better mobility in TGBC transistors (Figure 1b), which is consistent with literature reports.<sup>[37]</sup>

The mobility trend observed here is different from previous reports. N2200 films fabricated with the Langmuir–Schaefer method exhibited a decrease in mobility for thickness less than  $\approx 15 \text{ nm}$  (5 monolayers) when characterized in TGBC device configuration.<sup>[32]</sup> An inverse correlation of OFET mobility with thickness was also observed for other polymers.<sup>[41–43]</sup> It is, therefore, quite interesting to observe that N2200 ultrathin films show high mobility irrespective of device configuration.

### 2.3. Bulk Microstructure

To get better insight into the molecular packing of the thin films, we analyzed the films using grazing-incidence wide-angle X-ray scattering (GIWAXS).<sup>[44]</sup> The 2D GIWAXS patterns

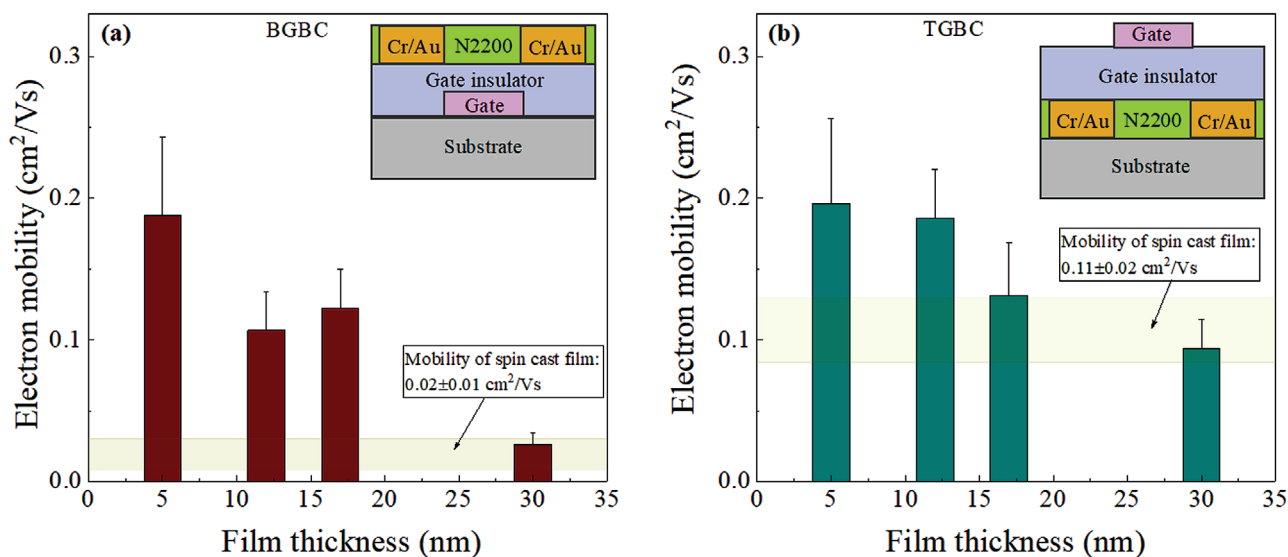


**Figure 1.** OFET mobility of a) bottom-gate bottom-contact, and b) top-gate bottom-contact devices as a function of the film thickness of floated films. The shaded areas show the mobility of 35 nm spin-cast films.

of the floated and spin-cast samples are shown in **Figure 2a–c** and their line cuts are displayed in **Figure 2d,e**. The 1D line-cuts of the ultrathin floated sample shows higher order lamellar stacking in the out-of-plane direction, indicating a more edge-on orientation. The properties of the molecular packing were explored further by exploring their in-plane  $\pi$ - $\pi$  stacking coherence length, which was obtained from fits (see **Figure S5**, Supporting Information) of the GIWAXS line cuts. The coherence length ( $L_c$ ) of the in-plane  $\pi$ - $\pi$  stacking is found to be the highest in the ultrathin floated film as listed in **Table 2**. The absolute value of the  $L_c$  of the 5 nm film could be debatable since the overlapping peaks affect the accuracy of the peak fitting (**Figure S5**, Supporting Information). However, the increasing trend of  $L_c$  with decreasing film thickness holds for the out-of-plane  $\pi$ - $\pi$  stacking as inferred from **Table 2**, confirming the trend achieved in the in-plane direction. The relative degree of crystallinity (rDoC)<sup>[45,46]</sup> was calculated using the (010) pole figure. The thickness and background normalized rDoC values are 0.61, 1.00, and 0.83 for the floated 5 nm, floated 12 nm, and spin-cast 35 nm films, respectively. The 12 nm floated film exhibits the highest rDoC, which indicates a more ordered film. Despite its lowest rDoC, the 5 nm floated sample exhibits the

**Table 1.** The electron mobility of bottom-gate bottom-contact (BGBC) and top-gate bottom-contact (TGBC) OFETs.

OFET type	Film thickness [nm]	Mobility [cm <sup>2</sup> V <sup>-1</sup> s <sup>-1</sup> ]
BGBC	5	0.19
BGBC	12	0.11
BGBC	17	0.12
BGBC	30	0.03
TGBC	5	0.23
TGBC	12	0.19
TGBC	17	0.13
TGBC	30	0.09

highest order lamellar stacking in comparison to the other two films. Moreover, as summarized in **Table 2**, the floated films show a lower  $\pi$ - $\pi$  stacking distance in the in-plane direction and a larger coherence length over the spin-cast films, with the 5 nm thick films exhibiting the smallest stacking distance and largest coherence length. A better in-plane paracrystalline order was achieved in the 5 nm film according to a paracrystallinity disorder parameter factor  $g$  (see **Table 2**) estimated as  $g = \frac{\Delta q}{q_0}$ , where  $q_0$  is the maximum peak position and  $\Delta q$  is the full width half maximum of the peak, and amorphous Si with a  $g$  parameter of 12% is considered as a reference.<sup>[45]</sup> A  $g$  parameter of less than 12% classifies polymers as semi-paracrystalline.<sup>[45]</sup> Here we have focused only on the in-plane (010) direction as it is more relevant for carrier mobility in OFET. Comparatively, only the 5 nm floated film has a  $g$  parameter of <12% and the other two have larger  $g$  parameters. This indicates that the 5 nm film has achieved a better order in the in-plane  $\pi$ - $\pi$  direction.

The lamellar stacking and the  $\pi$ - $\pi$  stacking in the 2D GIWAXS patterns were further analyzed using GIWAXS pole figure analysis (see **Figure S6**, Supporting Information)<sup>[47]</sup> to understand the orientation distribution of the films. The edge-on ( $A_E$ ) to face-on ( $A_F$ ) orientation ratio ( $A_E/A_F$ ) was obtained by integrating the (010) pole figure intensity with reference to the 45° azimuthal angles to obtain the intensity of a particular orientation (see **Figure 2f**), which is proportional to the population of that orientation. To obtain the  $A_E/A_F$  ratio, the signal from the volume fraction of molecules that are isotropically oriented was subtracted from the pole figure intensities following the best practice in the literature.<sup>[47]</sup> As inferred from **Figure 2f**, the ultrathin floated film (5 nm) is predominantly edge-on which is indicated by its significantly higher  $A_E/A_F$  ratio. It is noted that a thicker floated film exhibits an increased population of face-on orientation, and yet the spin-coated sample (35 nm) shows a relatively strong face-on orientation as determined from its low  $A_E/A_F$  ratio. This is further confirmed by the higher order

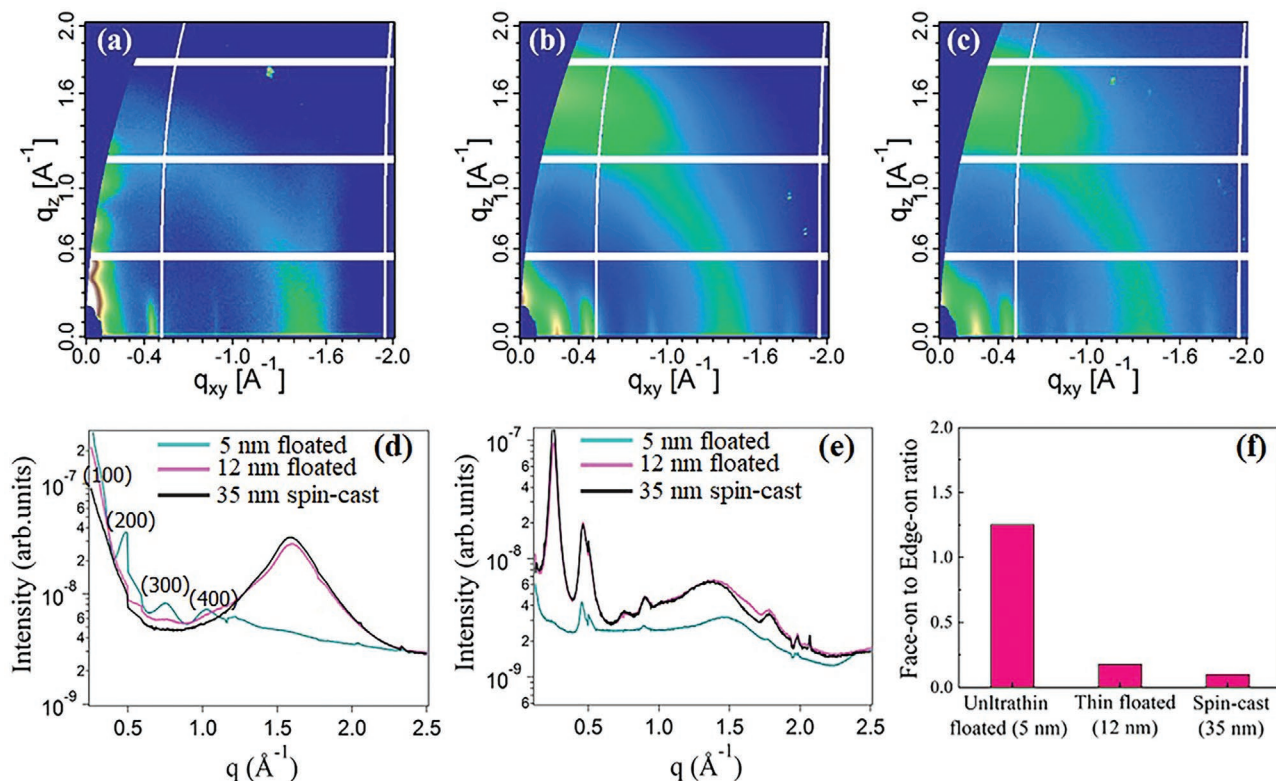


**Figure 2.** 2D GIWAXS patterns of a) floated 5 nm, b) floated 12 nm, and c) spin-cast 35 nm films. Corresponding d) out-of-plane, and e) in-plane GIWAXS 1D line-cuts of floated and spin-cast films. f) Edge-on to a face-on ratio ( $A_E/A_F$ ) of the water-floated and spin-cast films.

out-of-plane lamellar stacking in the 5 nm floated film, which is not visible in the other two films.

All parameters that can be extracted from GIWAXS, i.e., rDoC, stacking distance, coherence length, and texture, have been cited in the literature as being correlated to transport and performance. For example, a smaller  $\pi$ - $\pi$  stacking distance in the in-plane direction is considered to provide better charge transport across the stacking direction.<sup>[48,49]</sup> A large coherence length, which expresses the quality of ordering of the paracrystallites, is desired for efficient charge transport.<sup>[23,45,50]</sup> A strong long-range in-plane order in ultrathin polymer films is rarely reported.<sup>[34,38]</sup> Preferred edge-on orientation has long been argued to be beneficial for high mobilities in transistors. The relative contributions of these four factors are rarely disentangled. Here, we do not have enough data points to do so in a quantitative way. Overall, factors such as rDoC and stacking distance seem to play less important roles and the high mobility of the 5 nm thick

devices seem to be the results of the high preferential edge-on orientation and quality of  $\pi$ - $\pi$  ordering as captured by the largest coherence length.

## 2.4. Surface Morphology

Atomic force microscopy (AFM) images showing surface microstructural features of the floated films with varying thicknesses are displayed in **Figure 3**. As inferred from the AFM images, N2200 floated films form fibrillar-like structures on the surface of the film with some degree of orientation, which is typical for this material.<sup>[30,51]</sup> The polymer microstructures are more evident in the phase images (Figure 3d–f), with anisotropic fiber distributions. The surface morphology of the 35 nm spin-cast film (see Figure S7, Supporting Information) shows a close resemblance with the surface structure of the thick (30 nm) floated film. The room-mean-square surface roughness

**Table 2.** The GIWAXS parameters of the in-plane  $\pi$ - $\pi$  peak fittings of the films ( $\pi$ - $\pi$  stacking distance  $d$ , coherence length  $L_c$ ). The  $g$  parameters of the films, which indicate the paracrystalline order is also included.

Film type	Thickness [nm]	In-plane $\pi$ - $\pi$ stacking		Out-of-plane $\pi$ - $\pi$ stacking		g parameter [%]	
		$d$ [Å]	$L_c$ [Å]	$d$ [Å]	$L_c$ [Å]	In-plane	Out-of-plane
Ultrathin floated	5	3.93	50	3.89	30	11.20	14.60
Thin floated	12	3.93	26	3.93	20	15.40	17.80
Spin-cast	35	4.19	23	3.95	19	16.90	18.30

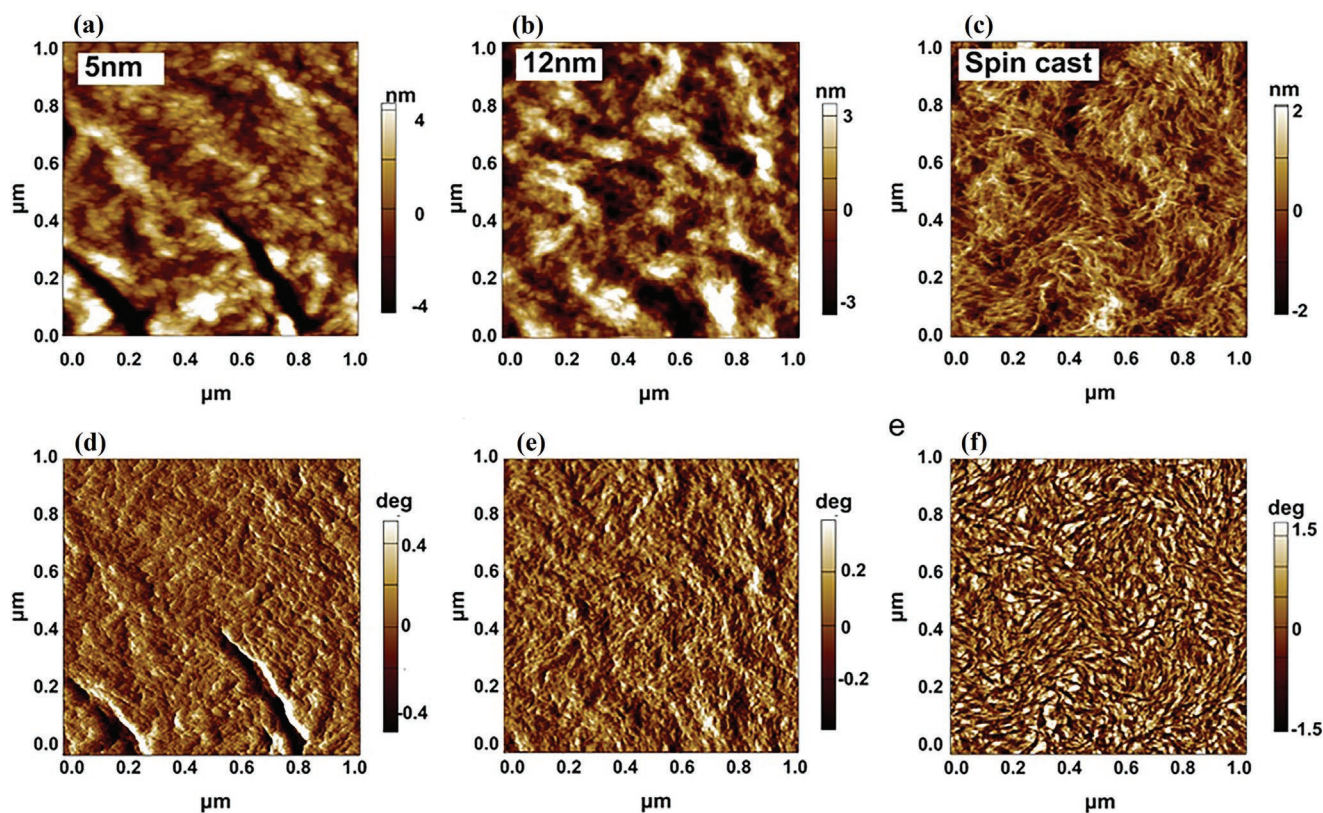


**Figure 3.** Topographic AFM height images of floated films of different thicknesses. a–c) Height images of 5, 12, and 30 nm thick films. d–f) Corresponding phase images of the 5, 12, and 30 nm.

of the films (Figure S8, Supporting Information) is 1.80, 1.68, and 0.70 nm for the floated 5, 12, and 30 nm films, respectively. The spin-cast film shows a roughness of 0.65 nm. The high roughness of the thinnest film may be attributed to its relatively higher degree of directional packing (i.e., edge-on crystals).<sup>[52]</sup>

We made further analysis of fiber dimensions by analyzing the real-space length scales of the thin films using power spectral density (PSD) analysis of the AFM phase images. The peaks shown in the PSD data (Figure 4) are related to the real space periodicity<sup>[53]</sup> of the surface of the film. The observed difference in the PSD profile is indicative of a varying length scale in materials order.

### 2.5. Optical Properties

The UV–vis absorption spectrum of N2200 floated and spin-cast films were characterized and depicted in Figure 5 and Figure S9 (Supporting Information). All films exhibit two distinct bands: the high-energy bands (near 3.2 eV), and the low-energy bands (1.75–1.77 eV), consistent with the literature.<sup>[54–58]</sup> According to the data presented in Figure 5a, the progression of the absorption spectra is dependent on film thickness particularly in high energy regions, which may be indicative of structural changes. A close look at the low energy peaks (Figure 5b) shows that the ultrathin film reveals a broad shoulder peak (1.55–1.63 eV), which is ascribed to aggregated chain segments.<sup>[56]</sup> On the other hand, it is noted that the 35 nm spin-cast film and the thickest floated sample (30 nm) exhibit similar optical properties.

### 3. Correlating the Microstructural and Electrical Properties

According to the charge transport studies, high electron mobility can be achieved in ultrathin floated films both in TGBC and BGBC transistors. Interestingly, nearly tenfold mobility can be achieved in BGBC devices utilizing ultrathin films compared to transistors with spin-coated films. The low mobility extracted from the BGBC N2200 transistor is a known

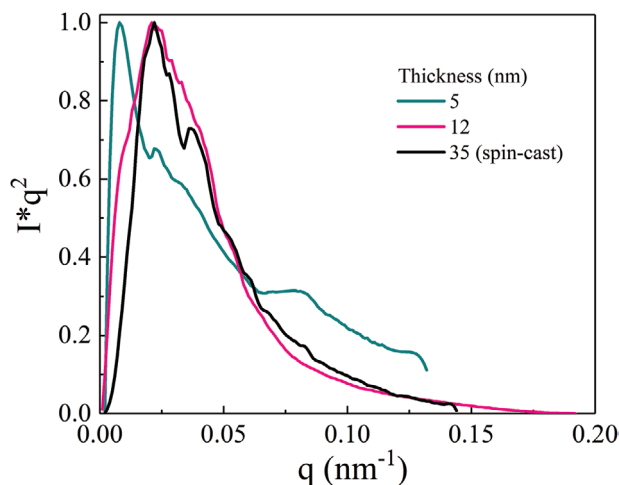


**Figure 4.** The PSD profiles as analyzed from the AFM phase images.

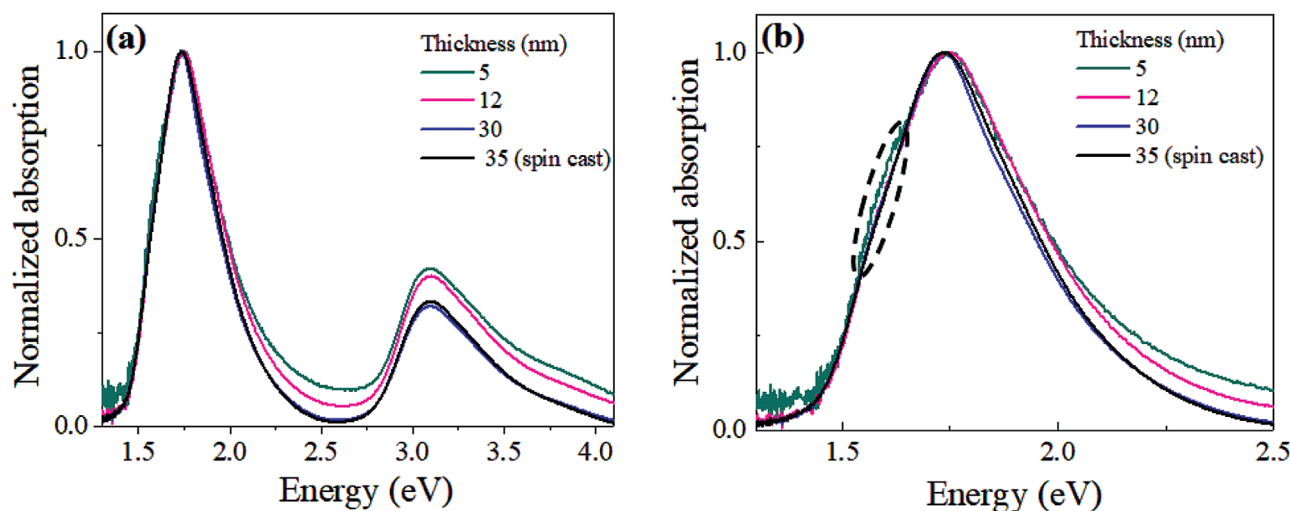


**Figure 5.** a) The normalized absorption spectra of N2200 films. b) The low energy band of the normalized absorption. The gray circle shows a vibration peak that is only clearly observed for the 5 nm film.

long-standing problem for spin-casted films, and this limitation is ascribed to the preferential edge-on orientation of the polymer chains only at the air interface.<sup>[38]</sup> Indeed, the strong edge-on orientation of the 5 nm floated film correlates well with its high OFET mobility while the decreased edge-on orientation in thicker films (Figure 2f) is accompanied by a drop in carrier mobility (Figure 1).

Given that the rDoC of the spin-coated film is relatively lower than the floated 12 nm sample, the volume fraction of the ordered aggregates in the thicker 35 nm sample should also be lower. On the other hand, even though the 5 nm film shows lower rDoC than the 12 nm floated film, its higher degree of the edge-on fraction of the aggregates has favorably improved electron mobility. This indicates that the edge-on oriented crystals can improve electron transport even in aggregates exhibiting low rDoC. The relatively smaller amount of aggregates in the perfect orientation have improved electron transport by facilitating highly connected percolation pathways. According to the GIWAXS analysis (Table 2), the coherence length of the ultrathin floated film is improved compared to the 12 nm floated and spin-cast films, indicating a relatively better quality of ordering of its paracrystallites, and this is indeed reflected in its  $<12\%$   $g$  parameter (Table 2). This is also consistent with the appearance of a shoulder peak in the optical transition of the ultrathin film (Figure 5b), indicative of aggregate formation. Besides, the PSD data revealed a larger length scale in the thinner film implying a larger fiber spacing and long-range order, which is known to be a recipe for efficient OFET charge transport.<sup>[59]</sup> It is noted that though the spin-cast film shows clear and thicker fibers in AFM images (Figure S7, Supporting Information) compared to the floated films, it gives comparatively lower charge mobility due to its unpreferred crystal orientations and lower order in its microstructures as witnessed in its small  $L_c$  as inferred from Table 2.

It can, therefore, be concluded that the preferred edge-on orientation together with the sufficiently large crystals of the ultrathin floated samples has improved its device mobility. In addition, the comparatively high mobility of the ultrathin film

regardless of OFET structure is indicative of the distribution of edge-on orientation throughout the film volume. The latter is a new observation for N2200. Fabiano et al. demonstrated high mobility in top-gate bottom-contact OFETs comprising a monolayer film of N2200 that is produced with the Langmuir–Schaefer deposition technique. They observed an increase in mobility as the number of layers increases, saturating with a mean value of  $0.018 \text{ cm}^2 \text{ V}^{-1} \text{ s}^{-1}$  at about 9 nm (three layers).<sup>[32]</sup> Our finding provides a means for the fabrication of ultrathin organic films characterized with efficient electrical properties due to an immediate realization of the desired film morphology. Moreover, our finding has an important implication for thin-film-based electronic devices. For example, in OFET chemical<sup>[5]</sup> and gas<sup>[60]</sup> sensors, ultrathin organic semiconductor films enhance response time significantly due to improved analyte motion to the sensing interface, whereas increased mobility is essential to achieve high sensitivity. We, therefore, believe that this work provides a vital guideline for the further development of next-generation sensors and flexible, wearable electronics.

#### 4. Conclusions

In this study, the electronic properties of ultrathin films of N2200 are explored in OFETs by considering films floated on the water surface. This research finds that ultrathin films ( $<10 \text{ nm}$ ) give high electron mobility in both BGBC and TGBC OFETs, while increasing film thickness lowers mobility. Such drastic changes in charge transport in thicker films reflect changes in the film microstructural features such as orientation at the device interfaces regardless of film-forming protocols. The ultrathin films retain a dominantly edge-on orientation and ordered morphology throughout the film volume, thus giving enhanced mobility in OFET regardless of device architecture. This finding unveils a spontaneous formation of favorable film structure in polymer ultrathin films, which is crucial for developing transparent and flexible electronics.

## 5. Experimental Section

**Sample Preparation:** The OFET substrates include a heavily doped Si base layer (500 nm) used as a bottom gate contact and a 300 nm thick layer of SiO<sub>2</sub> as the gate dielectric. To fabricate the transistor testbeds, Cr (10 nm)/Au (40 nm) contacts were formed through photolithography processes and thermal evaporation of the metals. Dual gate transistor structures encompassing both bottom-gate, and bottom-contact and top-gate bottom-contact structures were fabricated to measure charge transport at both interfaces. Before casting the polymer films, the substrates were cleaned with DI water, acetone, and isopropanol and subsequently treated with OTS to form a self-assembled monolayer following a previously used procedure.<sup>[59,61]</sup> The active layers were cast on water from a p-xylene solution and transferred to the transistor substrates by directly placing the substrates on the films. The resulting films were annealed at 110 °C in a nitrogen-filled glove box to dry the films. Film thicknesses were varied by changing solution concentration as well as the volume of solution dropped on the water substrate. To fabricate top-gated OFETs, CYTOP (Asahi Glass) was spin-coated on top of the N2200 films at 9000 rpm for 90 s resulting in a 500 nm dielectric layer. This was followed by annealing at 110 °C (4 h) before depositing a 40 nm thick Al gate through a shadow mask.

**Measurements:** The different characterization methods are given below.

**GIWAXS:** GIWAXS measurements were conducted at the Advanced Light Source (ALS), Lawrence Berkeley National Laboratory, Berkeley, CA at the beamline 7.3.3. Data were acquired at the critical angle (0.130) of the film with a hard X-ray energy of 10 keV. X-ray irradiation time was 10–30 s, depending on the saturation level of the detector. The Beam Center was calibrated using AgBr powder and the sample-to-detector distance was about 330 mm. The  $\pi$ - $\pi$  coherence lengths are estimated based on the Scherrer equation ( $L = 2\pi K/\text{FWHM}$ ), where  $K = 0.9$  is the shape factor, and FWHM is the full width at half maximum of the (010) diffraction peaks. The rDoC<sup>[45]</sup> was calculated using the (010) pole figure. The  $g$  parameter was also estimated according to the recent report.<sup>[45]</sup>

**AFM Measurements:** The AFM images were recorded using an Asylum research MFP-3D system in tapping mode.

**Absorption Spectrum:** The ex situ UV–vis spectra were recorded with Cary 60 spectrometer (Agilent).

**OFET I–V Characteristics:** The OFETs were characterized by a Keithley 4200 Semiconductor Parameter Analyzer. The parameter analyzer was coupled with triaxial feedthroughs with a Janis probe station, where the test samples were placed in a turbo-pumped vacuum chamber (10<sup>−5</sup> mbar). The device parameters were extracted from the transfer and output curves in the saturation regime.

## Supporting Information

Supporting Information is available from the Wiley Online Library or from the author.

## Acknowledgements

The authors gratefully acknowledge the support from the U.S. Office of Naval Research (ONR, Grant No. N000141712204) and the UNC General Administration Research Opportunity Initiative grant. X-ray data were acquired at beamline 11.0.1.2 and 7.3.3 at the Advanced Light Source, which is supported by the Director, Office of Science, Office of Basic Energy Sciences, of the U.S. Department of Energy under contract no. DE-AC02-05CH11231.

## Conflict of Interest

The authors declare no conflict of interest.

## Data Availability Statement

The data that support the findings of this study are available from the corresponding author upon reasonable request.

## Keywords

edge-on, mobility, transistor, ultrathin, water-processing

Received: December 5, 2021

Revised: February 6, 2022

Published online:

- [1] Y. Yao, H. Dong, F. Liu, T. P. Russell, W. Hu, *Adv. Mater.* **2017**, *29*, 1701251.
- [2] P. Hu, X. He, H. Jiang, *InfoMat* **2021**, *3*, 613.
- [3] X. Tao, V. Koncar, *Smart Textiles and Their Applications*, Elsevier, New York **2016**, p. 569.
- [4] Y. Li, X. Guo, Z. Peng, B. Qu, H. Yan, H. Ade, M. Zhang, S. R. Forrest, *Proc. Natl. Acad. Sci. USA* **2020**, *117*, 21147.
- [5] Y. Wang, J. Zhang, S. Zhang, J. Huang, *Polym. Int.* **2021**, *70*, 414.
- [6] M. H. M. Cativo, D. K. Kim, R. A. Riggelman, K. G. Yager, S. S. Nonnenmann, H. Chao, D. A. Bonnell, C. T. Black, C. R. Kagan, S.-J. Park, *ACS Nano* **2014**, *8*, 12755.
- [7] S. Oh, M. Yang, J. Bouffard, S. Hong, S.-J. Park, *ACS Appl. Mater. Interfaces* **2017**, *9*, 12865.
- [8] Y. Yang, Z. Liu, J. Chen, Z. Cai, Z. Wang, W. Chen, G. Zhang, X. Zhang, L. Chi, D. Zhang, J. Chen, L. Chi, Z. Cai, W. Chen, Y. Yang, Z. Liu, Z. Wang, G. Zhang, X. Zhang, D. Zhang, *Adv. Sci.* **2018**, *5*, 1801497.
- [9] Y. Sung, E.-Y. Shin, Y.-Y. Noh, J.-Y. Lee, *ACS Appl. Mater. Interfaces* **2020**, *12*, 25092.
- [10] J. Noh, S. Jeong, J.-Y. Lee, *Nat. Commun.* **2016**, *7*, 12374.
- [11] Y.-J. Kim, H.-T. Jung, C. W. Ahn, H.-J. Jeon, *Adv. Mater. Interfaces* **2017**, *4*, 1700342.
- [12] Y.-J. Kim, K. Park, H.-T. Jung, C. W. Ahn, H.-J. Jeon, *Cryst. Growth Des.* **2018**, *18*, 1261.
- [13] A. S. M. Tripathi, N. Kumari, S. Nagamatsu, S. Hayase, S. S. Pandey, *Org. Electron.* **2019**, *65*, 1.
- [14] Z. Wang, H. Dong, T. Li, R. Hviid, Y. Zou, Z. Wei, X. Fu, E. Wang, Y. Zhen, K. Nørgaard, B. W. Laursen, W. Hu, *Nat. Commun.* **2015**, *6*, 7478.
- [15] J.-H. Kim, C. Schaefer, T. Ma, J. Zhao, J. Turner, M. Ghasemi, I. Constantinou, F. So, H. Yan, A. Gadisa, H. Ade, *Adv. Energy Mater.* **2019**, *9*, 1802293.
- [16] J. C. Scott, J. D. J. Samuel, J. H. Hou, C. T. Rettner, R. D. Miller, *Nano Lett.* **2006**, *6*, 2916.
- [17] D. He, J. Qiao, L. Zhang, J. Wang, T. Lan, J. Qian, Y. Li, Y. Shi, Y. Chai, W. Lan, L. K. Ono, Y. Qi, J. Bin Xu, W. Ji, X. Wang, *Sci. Adv.* **2017**, *3*.
- [18] S. G. J. Mathijssen, E. C. P. Smits, P. A. Van Hal, H. J. Wondergem, S. A. Ponomarenko, A. Moser, R. Resel, P. A. Bobbert, M. Kemerink, R. A. J. Janssen, D. M. De Leeuw, *Nat. Nanotechnol.* **2009**, *4*, 674.
- [19] H.-R. Tseng, H. Phan, C. Luo, M. Wang, L. A. Perez, S. N. Patel, L. Ying, E. J. Kramer, T.-Q. Nguyen, G. C. Bazan, A. J. Heeger, *Adv. Mater.* **2014**, *26*, 2993.
- [20] C. Luo, A. K. K. Kyaw, L. A. Perez, S. Patel, M. Wang, B. Grimm, G. C. Bazan, E. J. Kramer, A. J. Heeger, *Nano Lett.* **2014**, *14*, 2764.
- [21] J. Yang, Z. Zhao, S. Wang, Y. Guo, Y. Liu, *Chem* **2018**, *4*, 2748.
- [22] K. Bulgarevich, K. Sakamoto, T. Minari, T. Yasuda, K. Miki, M. Takeuchi, *Adv. Funct. Mater.* **2019**, *29*, 1905365.
- [23] Z. Wang, X. Song, Y. Jiang, J. Zhang, X. Yu, Y. Deng, Y. Han, W. Hu, Y. Geng, *Adv. Sci.* **2019**, *6*, 1902412.

- [24] P. Yang, Y. Han, *Langmuir* **2009**, *25*, 9960.
- [25] P. K.-H. Ho, L.-L. Chua, M. Dipankar, X. Y. Gao, D. C. Qi, A. T.-S. Wee, J.-F. Chang, R. H. Friend, *Adv. Mater.* **2007**, *19*, 215.
- [26] M. Qian, Z. Song, G. Ding, Z. Hu, J. Liu, *RSC Adv.* **2019**, *9*, 28648.
- [27] H. Yang, R. Zhang, L. Wang, J. Zhang, X. Yu, J. Liu, R. Xing, Y. Geng, Y. Han, *Macromolecules* **2015**, *48*, 7557.
- [28] H. Sun, Q. Wang, J. Qian, Y. Yin, Y. Shi, Y. Li, *Semicond. Sci. Technol.* **2015**, *30*, 054001.
- [29] A. S. M. Tripathi, M. Pandey, S. Sadakata, S. Nagamatsu, W. Takashima, S. Hayase, S. S. Pandey, *Appl. Phys. Lett.* **2018**, *112*, 123301.
- [30] N. E. Persson, S. Engmann, L. J. Richter, D. M. DeLongchamp, *Chem. Mater.* **2019**, *31*, 4133.
- [31] N. Kumari, M. Pandey, H. Syafutra, S. Nagamatsu, M. Nakamura, S. S. Pandey, *ACS Appl. Mater. Interfaces* **2020**, *12*, 55033.
- [32] S. Fabiano, C. Musumeci, Z. Chen, A. Scandurra, H. Wang, Y.-L. Loo, A. Facchetti, B. Pignataro, *Adv. Mater.* **2012**, *24*, 951.
- [33] S. Wang, S. Fabiano, S. Himmelberger, S. Puzinas, X. Crispin, A. Salleo, M. Berggren, *Proc. Natl. Acad. Sci. USA* **2015**, *112*, 10599.
- [34] M. Li, D. K. Mangalore, J. Zhao, J. H. Carpenter, H. Yan, H. Ade, H. Yan, K. Müllen, P. W. M. Blom, W. Pisula, D. M. de Leeuw, K. Asadi, *Nat. Commun.* **2018**, *9*, 451.
- [35] V. D'Innocenzo, A. Luzio, H. Abdalla, S. Fabiano, M. A. Loi, D. Natali, A. Petrozza, M. Kemerink, M. Caironi, *J. Mater. Chem. C* **2016**, *4*, 11135.
- [36] J. Rivnay, R. Steyrleuthner, L. H. Jimison, A. Casadei, Z. Chen, M. F. Toney, A. Facchetti, D. Neher, A. Salleo, *Macromolecules* **2011**, *44*, 5246.
- [37] M. M. Nahid, A. Welford, E. Gann, L. Thomsen, K. P. Sharma, C. R. McNeill, *Adv. Electron. Mater.* **2018**, *4*, 1700559.
- [38] T. Schuettfort, L. Thomsen, C. R. McNeill, *J. Am. Chem. Soc.* **2013**, *135*, 1092.
- [39] W. D. Harkins, A. Feldman, *J. Am. Chem. Soc.* **2002**, *44*, 2665.
- [40] S. J. Kang, Y. Yi, C. Y. Kim, C. N. Whang, T. A. Callcott, K. Krochak, A. Moewes, G. S. Chang, *Appl. Phys. Lett.* **2005**, *86*, 232103.
- [41] S. Joshi, S. Grigorian, U. Pietsch, P. Pingel, A. Zen, D. Neher, U. Scherf, *Macromolecules* **2008**, *41*, 6800.
- [42] H. Jia, S. Gowrisanker, G. K. Pant, R. M. Wallace, B. E. Gnade, *J. Vac. Sci. Technol., A* **2006**, *24*, 1228.
- [43] D. Khim, G.-S. Ryu, W.-T. Park, H. Kim, M. Lee, Y.-Y. Noh, *Adv. Mater.* **2016**, *28*, 2752.
- [44] A. Hexemer, W. Bras, J. Glossinger, E. Schaible, E. Gann, R. Kirian, A. MacDowell, M. Church, B. Rude, H. Padmore, *J. Phys.: Conf. Ser.* **2010**, *247*, 12007.
- [45] Z. Peng, L. Ye, H. Ade, *Mater. Horiz.* **2022**, *9*, 577.
- [46] J. Rivnay, S. C. B. Mannsfeld, C. E. Miller, A. Salleo, M. F. Toney, *Chem. Rev.* **2012**, *112*, 5488.
- [47] K. A. Page, A. Kusoglu, C. M. Stafford, S. Kim, R. J. Kline, A. Z. Weber, *Nano Lett.* **2014**, *14*, 2299.
- [48] M. Bajpai, R. Srivastava, R. Dhar, R. S. Tiwari, *Mater. Sci. Eng., B* **2016**, *212*, 62.
- [49] J. M. Szarko, J. Guo, Y. Liang, B. Lee, B. S. Rolczynski, J. Strzalka, T. Xu, S. Loser, T. J. Marks, L. Yu, L. X. Chen, *Adv. Mater.* **2010**, *22*, 5468.
- [50] R. Di Pietro, T. Erdmann, J. H. Carpenter, N. Wang, R. R. Shivhare, P. Formanek, C. Heintze, B. Voit, D. Neher, H. Ade, A. Kiriy, *Chem. Mater.* **2017**, *29*, 10220.
- [51] J. Liu, L. Qiu, R. Alessandri, X. Qiu, G. Portale, J. Dong, W. Talsma, G. Ye, A. A. Sengrian, P. C. T. Souza, M. A. Loi, R. C. Chiechi, S. J. Marrink, J. C. Hummelen, L. J. A. Koster, *Adv. Mater.* **2018**, *30*, 1704630.
- [52] Y. J. Kim, S. Lee, M. R. Niazi, K. Hwang, M. C. Tang, D. H. Lim, J. S. Kang, D. M. Smilgies, A. Amassian, D. Y. Kim, *ACS Appl. Mater. Interfaces* **2020**, *12*, 36417.
- [53] S. J. Fang, S. Haplepete, W. Chen, C. R. Helms, H. Edwards, *J. Appl. Phys.* **1997**, *82*, 5891.
- [54] Y. Yan, Y. Liu, Q. Zhang, Y. Han, *Front. Chem.* **2020**, *8*, 394.
- [55] J. R. Moore, S. Albert-Seifried, A. Rao, S. Massip, B. Watts, D. J. Morgan, R. H. Friend, C. R. McNeill, H. Sirringhaus, *Adv. Energy Mater.* **2011**, *1*, 230.
- [56] R. Steyrleuthner, M. Schubert, I. Howard, B. Klaumünzer, K. Schilling, Z. Chen, P. Saalfrank, F. Laquai, A. Facchetti, D. Neher, *J. Am. Chem. Soc.* **2012**, *134*, 18303.
- [57] K. G. Jespersen, W. J. D. Beenken, Y. Zaushitsyn, A. Yartsev, M. Andersson, T. Pullerits, V. Sundström, *J. Chem. Phys.* **2004**, *121*, 12613.
- [58] G. Wen, X. Zou, R. Hu, J. Peng, Z. Chen, X. He, G. Dong, W. Zhang, *RSC Adv.* **2021**, *11*, 20191.
- [59] I. Angunawela, M. M. Nahid, M. Ghasemi, A. Amassian, H. Ade, A. Gadisa, *ACS Appl. Mater. Interfaces* **2020**, *12*, 26239.
- [60] L. Li, P. Gao, M. Baumgarten, K. Müllen, N. Lu, H. Fuchs, L. Chi, *Adv. Mater.* **2013**, *25*, 3419.
- [61] X. Xue, G. Chandler, X. Zhang, R. J. Kline, Z. Fei, M. Heeney, P. J. Diemer, O. D. Jurchescu, B. T. O'Connor, *ACS Appl. Mater. Interfaces* **2015**, *7*, 26726.